J. Ocean Univ. China (Oceanic and Coastal Sea Research)
https://doi.org/10.1007/s11802-025-6130-6
ISSN 1672-5182, 2025 24 (6): 1596-1612
http://www.ouc.edu.cn/xbywb/
E-mail:xbywb@ouc.edu.cn

Main Controlling Factors of Imbricate Thrust Faults at the Frontal Edge of the Makran Accretionary Wedge–Insights from Physical Simulations

SUN Bo[1)], YU Fusheng[1), 2), *], LIAO Jing[3)], GONG Jianming[3)], YAN Jiajie[1)], LEI Wenhao[1)], QU Jiajun[1)], SUN Haoyue[1)], CUI Zixuan[1)], and REN Jia[1)]

1) *College of Geosciences*, *China University of Petroleum* (*Beijing*), *Beijing* 102249, *China*
2) *State Key Laboratory of Petroleum Resources and Engineering*, *Beijing* 102249, *China*
3) *Qingdao Institute of Marine Geology*, *China Geological Survey*, *Qingdao* 266071, *China*

(Received January 10, 2025; revised March 17, 2025; accepted March 28, 2025)

Abstract The frontal edge of the Makran accretionary wedge is characterized by the development of multiple imbricate thrust faults trending E-W and relatively parallel. However, the mechanisms underlying their formation and the factors controlling their development remain subjects of debate. This paper, based on seismic profile analysis, employs physical simulation experiments to establish a 'wedge' type subduction model. The study explores the influence of the initial wedge angle, horizontal sand layer thickness, and the presence or absence of a decollement layer on the structural styles of the thrust wedge. Experimental results indicate that as the initial wedge angle decreases from 11° to 8°, the lateral growth of the thrust wedge increases, whereas vertical growth diminishes. When the horizontal sand layer thickness is reduced from 4.5 cm to 3.0 cm, the spacing between the frontal thrusts decreases and the number of thrust faults increases. Both lateral and vertical growth are relatively reduced, resulting in a smaller thrust wedge. When a decollement layer is present, the structural style exhibits layered deformation. The decollement layer constrains the development of back thrusts and promotes the localized formation of frontal thrusts. In conclusion, the imbricate thrust faults at the frontal edge of the Makran accretionary wedge are primarily controlled by the characteristics of the wedge itself and the presence of the decollement layer.

Key words Makran accretionary wedge; imbricate thrust faults; mechanisms; PIV technique; physical simulation

1 Introduction

The Makran accretionary wedge is a typical geological structure formed by the subduction of the Arabian Plate beneath the Eurasian Plate. This geological feature extends approximately 1000 km in an E-W direction along its strike, with the deformation front located about 150 km from the coastline. In this region, numerous imbricate thrust faults, relatively parallel and evenly spaced, have developed along an E-W orientation (Kopp *et al*., 2000; Cromie *et al*., 2022). These faults are closely associated with the formation of natural gas hydrate reservoirs and are typically linked to the characteristics of the bottom simulating reflector (BSR) observed in seismic sections (von Rad *et al*., 2000; Ding *et al*., 2010; Smith *et al*., 2014; Meng *et al*., 2019; Liao *et al*., 2022; Qian *et al*., 2022). At active convergent plate boundaries, the crustal lithosphere forms a structural wedge *via* thrusting. The structural styles of such wedges have been investigated through sandbox experiments, revealing typical deformation features such as edge indentations, uplift, subsidence, back thrusts, and strike-slip faults (Lallemand *et al*., 1992; Dominguez *et al*., 1998; Hampel *et al*., 2004). The spacings and shapes of deep thrust faults in the Makran accretionary wedge are constrained by the decollement layer. Shallow normal faults are formed by the rapid upwelling of mud diapirs or the rapid uplift of thrust fault-related folds, resulting in tensile fractures in the upper strata or even the collapse of these strata (Shao *et al*., 2024). Gong *et al*. (2016) claimed that the northward subduction at a small angle resulted in the parallel arrangement of the E-W oriented thrust faults in the Makran accretionary wedge. Smith *et al*. (2012) stated that the collision of the Murray Ridge led to a slight deflection of the eastern fault toward the northeast. The formation of diapirs associated with wedge development was triggered by overpressure generated by wedge-induced loads and the downward subduction of the basement. The uplift rate of fault-propagation folds at the frontal region of the Makran accretionary wedge exceeds the sedimentation rate, indicating active thrusting at the wedge front (Grando and McClay, 2007). However, the mechanisms governing the formation of thrust faults within the Makran accretionary wedge

* Corresponding author. E-mail: fushengyu@cup.edu.cn

and the factors that control them remain inadequately understood. Critical wedge theory has been successfully employed to explain the mechanical characteristics of fold-thrust belts, forearc wedges, and orogenic belts (Davis *et al*., 1983; Platt, 1986; Willett, 1992). The spacing of thrust faults at the wedge front increases in response to the enhancement of basal friction (Wang, 1995); and erosional processes limit the advancement and thickening of the wedge, localizing deformation (Avouac and Burov, 1996; Hoth, 2005; Konstantinovskaia and Malavieille, 2005; Hoth *et al*., 2006). This study, based on seismic reflection data, investigates the effects of the initial wedge angle, the thickness of horizontal sand layer, and the presence or absence of a decollement layer on the structural style of thrust faults in the accretionary wedge using physical simulation experiments.

2 Geological Setting

The Makran accretionary wedge is located in the northern Arabian Sea, at the junction of the Eurasian, Arabian, and Indian Plates. To the west, it borders the Zagros collision zone, while to the east, it adjoins the Himalayan collision zone (Burg, 2018). The Makran accretionary wedge extends from approximately 57°30′E in southeastern Iran to 66°30′E in southern Pakistan, spanning a total length of about 1000 km. Its topographic range varies from 3000 m below sea level to 1500 m above sea level. The North Makran tectonic units are derived from the North Makran Ocean and the Neo-Tethys through two distinct northward dipping subduction events, without any intervening microcontinent (Barbero *et al*., 2025). The subduction rate is 3.65 cm/yr in the western section and 4.2 cm/yr in the eastern section (as shown by the black arrows in Fig.1a; DeMets *et al*., 1990). The region is characterized by extensive BSR, indicating a substantial potential for natural gas hydrates (Gaedicke *et al*., 2002; Smith *et al*., 2012). Well-developed tight anticlines and imbricate thrust faults are aligned in an E-W direction. The accretionary wedge spans approximately 500 km from north to south, with some offshore areas exceeding 100 km in width. The maximum sediment thickness exceeds 7000 m, especially in the central and eastern parts (White and Klitgord, 1976; Kopp *et al*., 2000; Kukowski *et al*., 2001; Gong *et al*., 2016; Cromie *et al*., 2022). The collision between the Arabian and Eurasian Plates began in the Cretaceous, and the development of the accretionary wedge commenced in the Oligocene (Platt *et al*., 1985; Fruehn *et al*., 1997; Liao *et al*., 2019). This convergence is associated with the northward subduction of the Neo-Tethys Ocean beneath the Eurasia Plate margin (Platt *et al*., 1985; Burg, 2018; Monsef *et al*., 2018; Saccani *et al*., 2018). The wedge is bounded to the west by the Minab dextral strike-slip fault system and to the east by the Ornach-Nal sinistral strike-slip fault system, separating it from the active continental collision zones of the Zagros and the Himalayas (Grando and McClay, 2007). Since the Miocene, the tectonic evolution of the Makran accretionary wedge has been marked by the gradual uplift of the northern region, southward propagation of thrust faults, weakening of tectonic activity in the north, and the formation of new thrust faults in the south (Arthurton *et al*., 1982; Harms *et al*., 1984; Platt *et al*., 1985).

Ellouz-Zimmerman (2007) established the stratigraphic framework of the Makran accretionary wedge in Pakistan, dating back to the Oligocene. Overall, the Makran accretionary wedge consists of a sedimentary sequence of deep-sea turbidites, deep-water mudstones, and shallow marine sandstone-mudstone facies, which are divided into three major sequences (Fig.2). The upper part of Sequence I exhibits strong reflectors, whereas the lower part shows weak reflectors. This corresponds to the Hoshab-Panjgur formation, which primarily comprises mudstones and turbidites, with mud diapir structures. Sequence II represents piggyback basin deposits, mainly composed of sandstones, corresponding to the late Miocene to early Pliocene. In this sequence, the strata are nearly horizontal in the shelf area and dip northward in the slope area, with thrust faults developing synchronously during deposition. Sequence III is wedge-shaped, and primarily consists of mudstones, sandstones, and siltstones, corresponding to the Hinglaj-Ormara formation. It is characterized by submarine landslides and canyons, indicating an abundant and unstable sediment supply. The formation of Sequences I to III reflects the evolution of the depositional environment and the influence of thrust faults and mud diapir structures on the sedimentary sequences, offering significant geological evidence for understanding the thrust faults in the Makran accretionary wedge.

3 Data and Methodology

This study primarily relies on 2D seismic reflection data provided by the Government of Pakistan to assist in interpreting the development of the thrust wedge. The 2D seismic reflection data encompasses approximately 54000 km^2 within the Makran accretionary wedge and includes a total of 49 seismic lines (Fig.1). The spacing between the N-S seismic lines ranges from 10 to 15 km, while that between the E-W seismic lines ranges from 10 to 25 km. Four N-S seismic profiles, perpendicular to the strike of the thrust faults, were selected to delineate the distribution and structural characteristics of these faults.

Based on the interpretation of the seismic profiles, this study employed physical simulation experiments to establish a ‘wedge-type’ subduction model. Particle image velocimetry (PIV) was employed to analyze the velocity field during the planar evolution of the experiments. Four sets of sandbox physical simulation experiments were designed. Experiment 1 served as the compared group, while Experiments 2, 3, and 4 investigated the effects of the initial wedge angle, horizontal sand layer thickness, and the presence or absence of a decollement layer on the structural style of the thrust wedge. In Experiment 2, the initial wedge angle was decreased from 11° to 8°; in Experiment 3, the thickness of the horizontal sand layer was reduced from 4.5 cm to 3 cm; and in Experiment 4, micro glass beads were added to the horizontal sand layer to

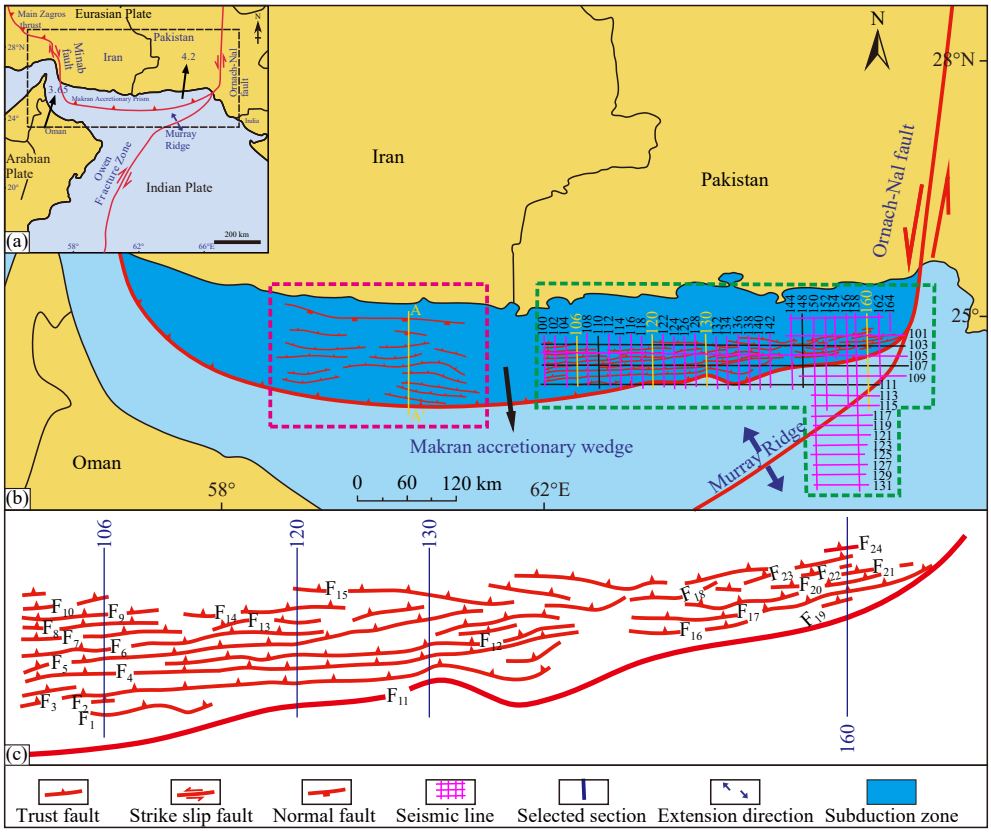

Fig.1 Regional tectonic setting of the Makran subduction zone (Grando and McClay, 2007). (b) is the enlargement of the black dotted box in (a); (c) is the enlargement of the north-dipping reverse fault in the green dashed box of the (b). The fault distribution in the pink dotted box is from Grando and McClay (2007); in the green dotted line frame is the seismic work area of this paper, and the faults distribution after Smith *et al.* (2012).

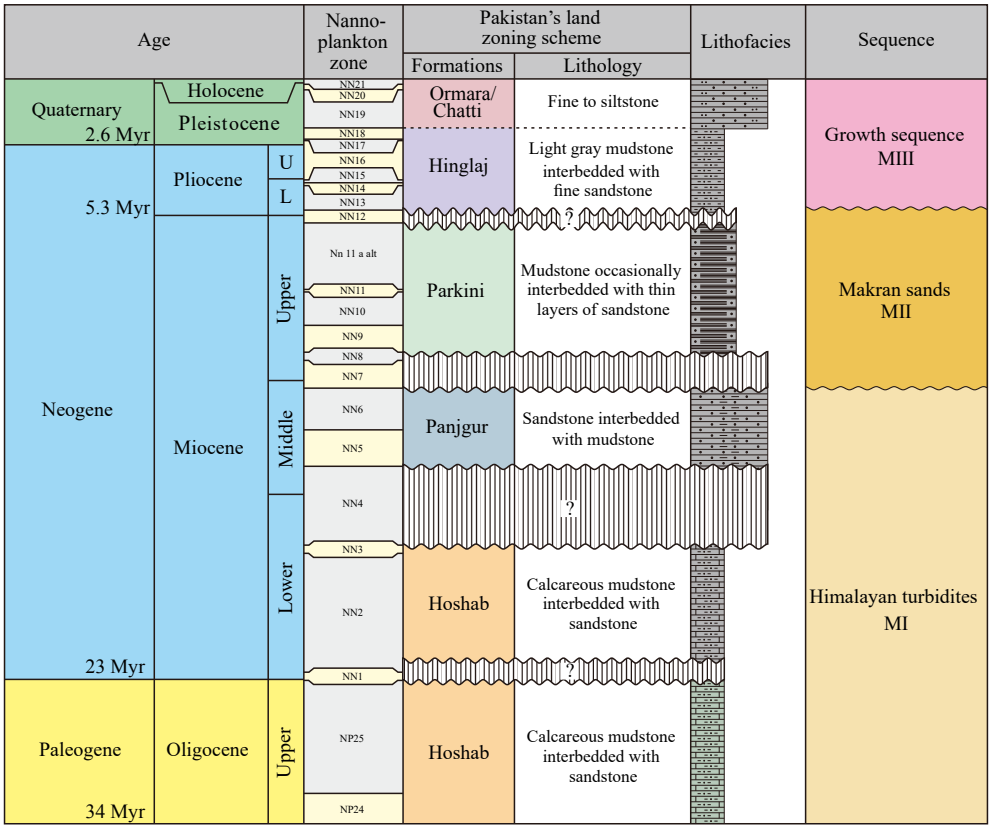

Fig.2 Composite stratigraphic column of the Makran Subduction Zone (modified from Ellouz-Zimmerman *et al.*, 2007; Khan *et al.*, 2015; Liao *et al.*, 2019).

simulate a decollement layer. The simulation results were then compared with actual seismic profiles to identify the primary controlling factors influencing the formation of imbricate thrust structures at the frontal edge of the Makran accretionary wedge.

3.1 Material Selection

The materials employed in this experiment include dry, loose quartz sand and micro glass beads. Dry, loose white and grey quartz sand is employed to simulate the brittle Coulomb behavior of the crust, with colored quartz sand serving as a marker layer. The quartz sand has a grain size of 300–450 μm, a density of 1.35 g/cm^3, and exhibits nearly zero cohesion. Its deformation properties follow the Coulomb criterion, with an internal friction angle of approximately 31°, which is similar to the internal friction angle of upper crustal rocks (with a thickness of less than 10 km). This makes it an ideal material for simulating brittle deformation in the upper crust (Koyi *et al.*, 1993; Yu *et al.*, 2019). Additionally, micro glass beads are employed to simulate the plastic layer in the lower part of the study area. The micro glass beads have a grain size of 100–200 μm, exhibit excellent sorting and rounding, and have a density of 1.45 g/cm^3, with cohesion between 46 and 51 Pa, which is almost negligible. Compared to granular sand, micro glass beads have lower mechanical strength, making them suitable for simulating weak layers found in nature (Cotton *et al.*, 2000; Yu *et al.*, 2012; Yu *et al.*, 2022).

3.2 Experimental Device and Methodology

The experimental device and materials was designed based on a comprehensive analysis of natural conditions, with full consideration given to the physical properties of various rocks in the lithosphere. As shown in Fig.3, the experimental device includes components such as a drive motor, conveyor belt, lifting motor, backstop, transparent glass side wall, and wedge-shaped track. In Fig.3a, the quartz sand used in the simulation experiment is evenly distributed on the conveyor belt, with the wedge stopper formed by piled quartz sand and the backstop remaining in a fixed position. The conveyor belt moves from right to left, driven by a drive motor, and the sand layer gradually advances, forming a new thrust wedge. The conveyor belt represents the oceanic plate, while the sand layer on the belt simulates sediments deposited on the oceanic plate. In Fig.3b, the sand layer is laid in two stages: the first stage involves laying a horizontal sand layer without the wedge-shaped track, while the second stage creates a wedge-shaped sand layer after the wedge-shaped track is installed.

The refined seismic stratigraphy of the sequence and the clear imaging of frontal deformation structures in the profiles enables improved identification of the inter plate thrust where it is propagating into the trench sediments. The interpolated thrust is recognized as the major decollement, above which the accreted sequence is shortened by distributed thrust faulting and folding, and below, undeformed sediments are subducted. Near the front of the wedge, the stratigraphic position of the decollement is tightly constrained within a couple of wavelets of the seismic data, based on the down-dip extent of the accretionary thrusts observed from inclined hanging wall reflections and footwall reflection cutoffs.

The thickness of the micro glass beads was determined based on detailed studies of actual geological conditions and the specific physical properties of these beads in experimental settings, including seismic profile analysis and scientifically derived model scaling ratios. Specifically, the selected thickness was guided by the depth ranges of key reflective interfaces identified in seismic profiles and adjusted according to the geometric scaling ratio of the model, ultimately set at 1 cm. This configuration effectively simulates the physical characteristics and sedimentary thickness variations of the target strata.

Four sets of experiments were designed in this study,

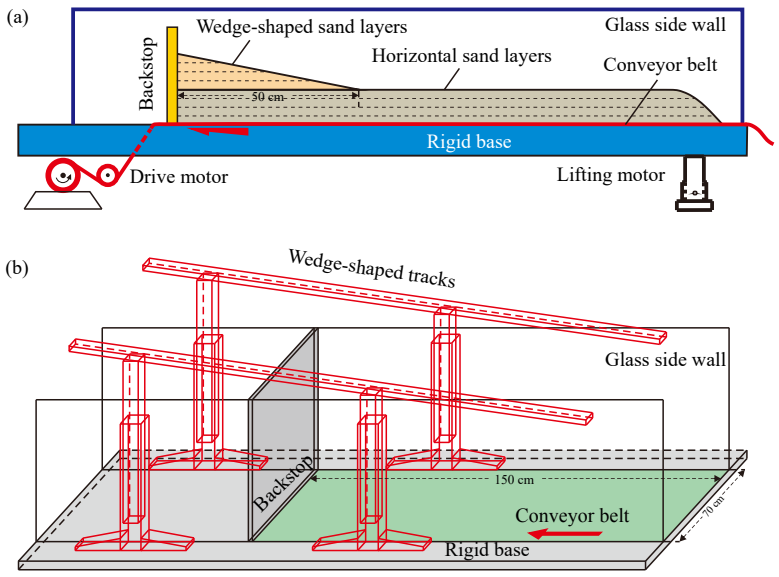

Fig.3 Schematic diagram of experimental device. (a), two-dimensional view of the experimental device; (b), three-dimensional view of the experimental device.

with each experimental area measuring 150 cm×70 cm. The specific sand layer configurations for each experiment are shown in Fig.4. The subduction angle for all four experimental models was set at 3°, the subduction rate of the experimental setup was 0.3 cm/min, and the final subduction distance was 35 cm. Detailed parameters are listed in Table 1. Throughout the experiment, high-definition cameras captured both plan and profile views of the experimental model every 15 s, enabling observation and recording of deformation characteristics.

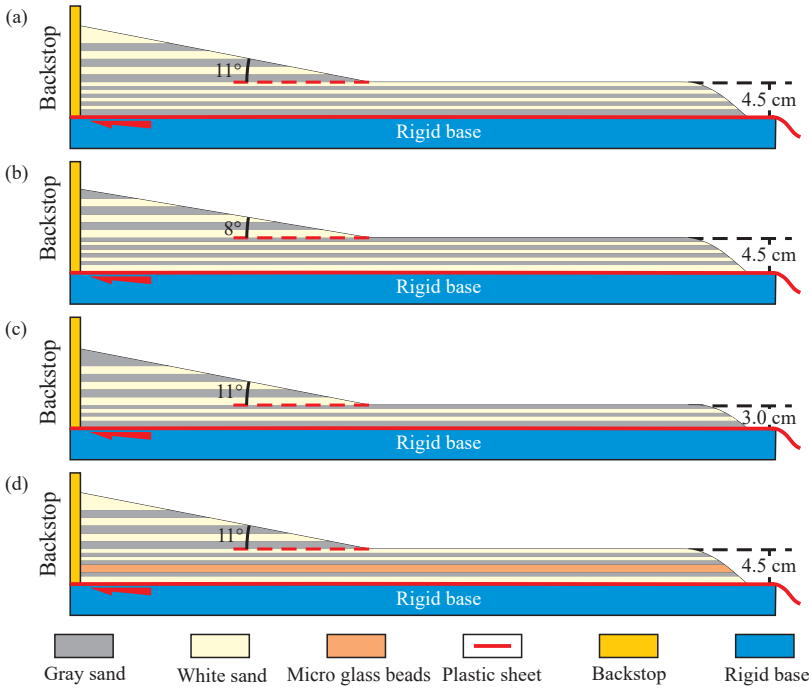

Fig.4 Layout of the experimental sand layers in Experiment 1 (a), Experiment 2 (b), Experiment 3 (c), and Experiment 4 (d).

Table 1 Experimental parameters

Experimental group	Wedge angle (°)	Micro glass beads	Total thickness of the horizontal layer	Shortening rate (cm/min)	Total shortening (cm)	Subduction angle (°)
Experiment 1	11	No	4.5	0.3	35	3
Experiment 2	8	No	4.5	0.3	35	3
Experiment 3	11	No	3.0	0.3	35	3
Experiment 4	11	Yes	4.5	0.3	35	3

3.3 Experimental Principles

The objective of this experiment is to investigate the formation and evolution of the front edge of the wedge structure in a subduction zone. This model is based on the work of Davis *et al.* (1983) (Fig.5). Based on the critical wedge mechanical equilibrium conditions and assuming that wedge deformation adheres to the Coulomb failure criterion, Davis *et al.* (1983) derived the critical wedge theory formula (Eq. (1)), accounting for both terrestrial and marine conditions. In the sandbox physical simulation experiment employing dry quartz sand, the pore fluid pressure ratio (λ) within the wedge and the fluid pressure ratio (λ_b) in the decollement layer are set to 0, thereby simplifying Eq. (1) to Eq. (2). The characteristics of the wedge are primarily controlled by the following factors: 1) surface slope α; 2) basement slope β; and 3) friction coefficient of the basal decollement μ_b.

$$\alpha+\beta=\frac{(1-\lambda_b)\mu_b+(1-\rho_w/\rho)\beta}{(1-\rho_w/\rho_w\rho)+(1-\lambda)K}, \tag{1}$$

$$\alpha+\beta=\frac{\mu_b+\beta}{1+K}. \tag{2}$$

These formulas are referenced in order to apply the cri-

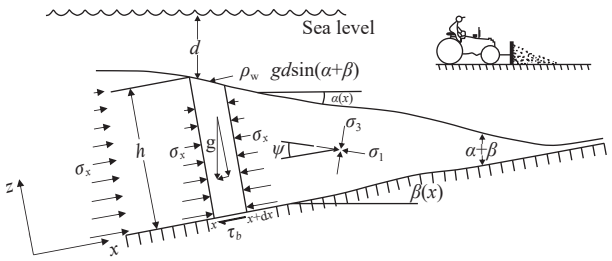

Fig.5 Schematic diagram of a wedge subject to horizontal compression following the Coulomb failure criterion. d, water depth above the wedge; h, height of the wedge; g, gravitational acceleration; ρ_w, water density; τ_b, shear traction; σ_x, normal traction across any plane perpendicular to the x-axis; σ_1, σ_3, maximum and minimum effective compressive stresses, respectively; ψ, angle between σ and the x-axis; α, surface slope of the wedge; β, dip angle of the base of the wedge.

terion for constructing wedge-shaped bodies during the initial stages of each of the four experiments. This model represents only the overall macroscopic mechanics, leaving out the complex internal structures or specific deformation phases of the wedge. In the experimental model, 1 cm represents 1 km in the real model, with specific scale parameters listed in Table 2.

Table 2 Scale parameters of the model

Scaling parameter	Model	Nature	Model/ nature ratio
Length (m)	0.01	1000	1.0×10^{-5}
Gravitational acceleration, g (m/s)	9.81	9.81	1
Density of sand (g/cm)	2.3	–	–
Density micro glass bead (g/cm)	1.45	–	–
Grain shape	Well-rounded	–	–
Friction angle (°)	36	40	0.9

4 Analytical Results

4.1 Structural Pattern of Thrust Faults

4.1.1 Distribution of thrust faults

The north-south seismic profile A–A′, located in the central-western offshore Makran accretionary wedge, spans approximately 120 km and crosses the major geomorphic structures of the wedge (Fig.6). Based on the A–A′ seismic profile, the N-S Makran accretionary wedge can be divided into three distinct zones: 1) The lower slope zone, 50–60 km wide, with an overall surface slope of 1° to 2°. Thrust faults are primarily concentrated near the abyssal plain, exhibiting fault propagation folds and imbricate fan structures; 2) The middle slope zone, spanning 15–20 km, features flat topography with a surface slope not exceeding 1°. However, the flanks of the mid-slope ridge, particularly near the lower slope, display steeper dips. Thrust faults are relatively sparse, but these faults are often associated with diapiric structures, forming a distinct middle slope ridge; 3) The upper slope zone extends 40 km towards the shelf, with a surface slope of approximately 7°. The topography is rough and uneven, with significant sediment accumulation. Near the shelf edge, normal faulting is also observed and manifests as either small-offset normal faults or large listric normal faults, that is deeply rooted growth faults resulting from gravity sliding over detachments, which are likely associated with local overpressure conditions at depth. These normal faults have been documented in both the Iran and Pakistan sectors of the Makran (Ellouz-Zimmerman *et al.*, 2007; Grando and Mclay, 2007). Interpretation of the relatively shorter north-south seismic profile in the eastern region (approximately 70 km long, Fig.7) reveals that the number of thrust faults gradually decreases from west to east (Fig.7).

In plan view, the thrust faults are generally oriented in an E-W direction, aligning parallel to the primary direction of tectonic movement. Owing to the higher convergence rate in the eastern region, the density and activity of thrust faults are significantly higher compared to the western region (Fig.1b). Additionally, the distribution of thrust faults is influenced by strike-slip faults, particularly near the Ornach-Nal sinistral strike-slip fault zone in the east, where normal faults have developed (Platt *et al.*, 1985). The formation of these normal faults is primarily attributed to flexural processes and is independent of the thrust faults (Fig.7d).

4.1.2 Thrust fault systems and deformation patterns

The thrust faults in the Makran accretionary wedge exhibit diverse geometries and structural characteristics, indicating the complex tectonic processes shaping the wedge. In the imbricate fan structure of the lower slope zone, thrust faults develop into a series of fault propagation folds. These thrust faults do not typically breach the seafloor but rather terminate in asymmetrical fault propagation folds, which commonly verge southward, with a steeper rear limb and a gentler forelimb. The formation of these folds is closely associated with the rotation of the thrust faults. Deep thrust faults are connected to shallow extensional faults through soft linkages (Fig.7), forming a ‘relay’ transport pathway (Gong *et al.*, 2018b; Meng *et*

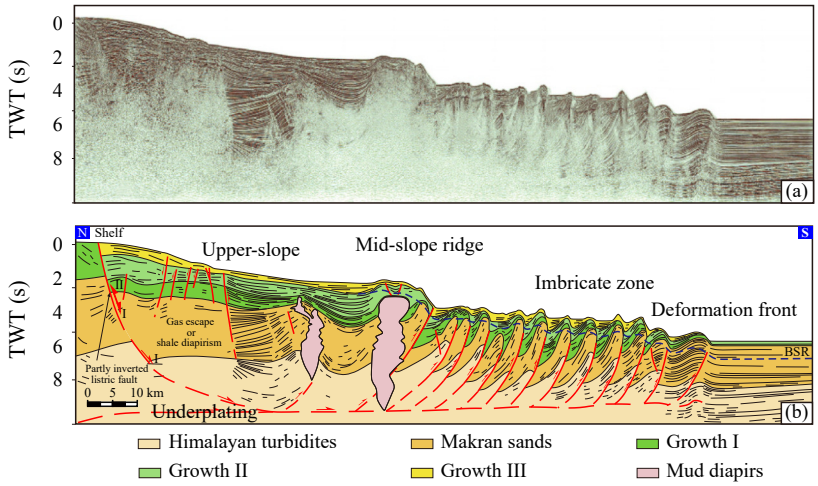

Fig.6 (a), A–A′ seismic section in the western segment of the Makran accretionary wedge. (b), interpretation of the seismic profile in (a). Fig.1 shows the location of the A–A′ seismic section, with reference to Grando and McClay (2007).

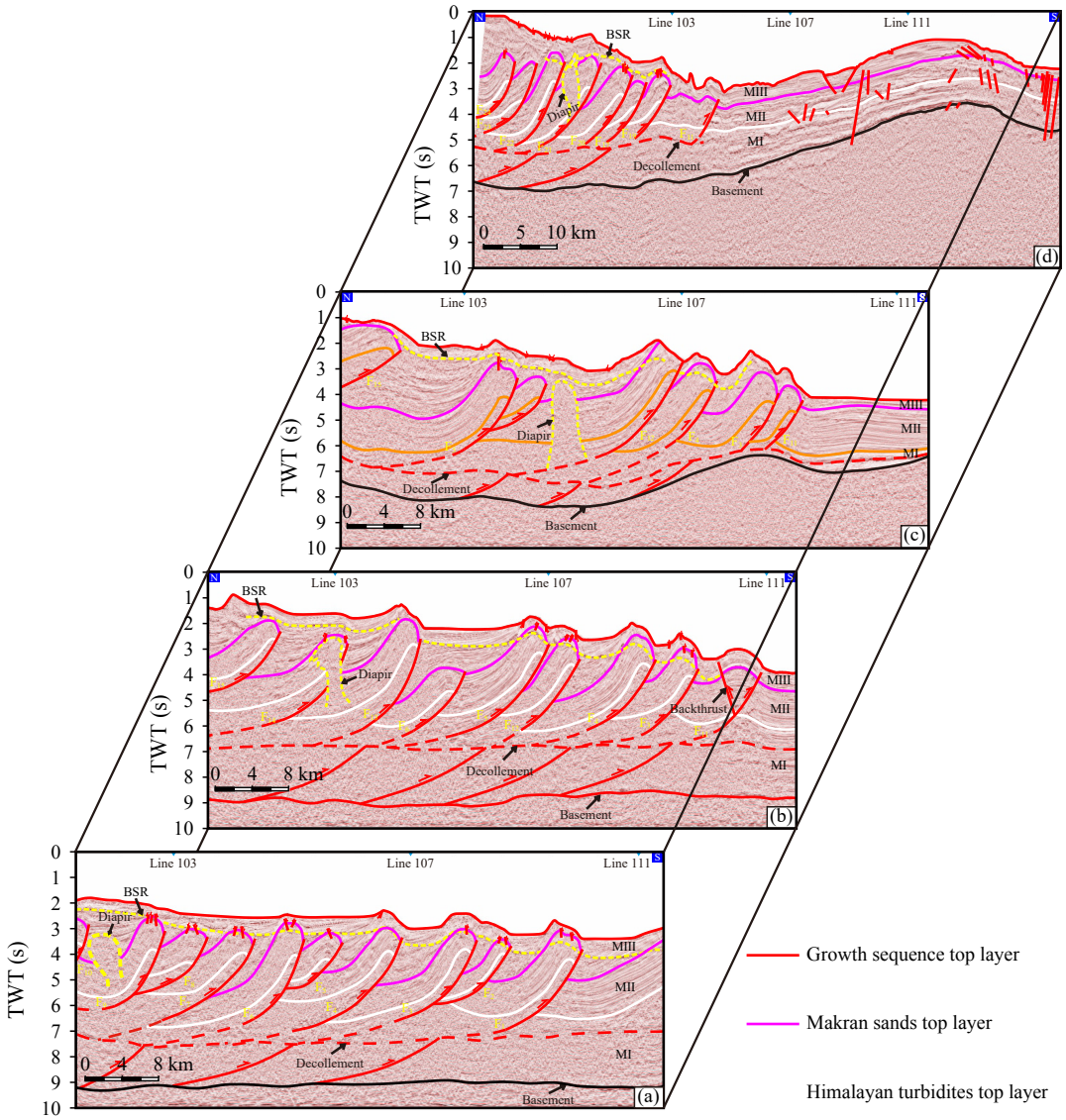

Fig.7 S-N seismic composite sections of the Makran accretionary wedge (modified from Shao *et al.*, 2024). (a), line 106 seismic interpretation section; (b), line 120 seismic interpretation section; (c), line 130 seismic interpretation section; (d), line 160 seismic interpretation section. Fig.1 shows the locations of seismic lines 106, 120,130 and 160.

al., 2019).

Piggyback synclinal basins, formed between thrust faults, are typically filled with relatively recent sediments and exhibit distinct growth strata sequences. This suggests that the formation of these basins is synchronous with thrust fault activity. The thickness and sedimentation rate of these basins are controlled by the intensity of thrust fault activity. In the upper slope region, near the edge of the shelf, listric normal faults have developed (Fig.6), with fault planes intersecting the Himalayan turbidite sequence at depth. As subduction progresses, these listric normal faults undergo slight tectonic inversion, resulting in partial compression of the overlying strata along the fault planes. This inversion phenomenon demonstrates the alternation of extensional and compressional forces acting within the Makran accretionary wedge during plate subduction. As new thrust faults form at the wedge front, the rear thrust faults typically rotate backward, steepening the fault planes and reducing the spacing between faults.

The thrust faults in the Makran accretionary wedge are widespread and exhibit intricate structural characteristics. Layered deformation features are observed above and below the detachment layer, with thrust faults converging downward into the lower detachment layer. Beneath the detachment layer, a few small-scale thrust faults are developed (Fig.7). Their formation is closely associated with plate convergence, sedimentation rates, diapirism, and other factors, all playing a key role in the structural evolution of the wedge. The partial inversion of listric normal faults, alongside the development of normal faults at the top, further reveals how changes in the tectonic stress field influence the structural style of the wedge in a complex subduction environment.

4.2 Physical Simulation Experiments

The four sandbox experiments described in this paper experienced deformation under various subduction modes

(Figs.8–11). During the evolutionary process, initial deformation was triggered at the frontal base of the wedge (hinge region) in all cases (McClay and Whitehouse, 2004). The initial deformation in Experiments 1, 2, and 3 was characterized by pop-up structures, which expanded and became asymmetric during subduction, accompanied by the development of back thrust faults. Eventually, this led to the formation of a thrust wedge composed of multiple imbricate thrust belts. In Experiment 4, the initial deformation was characterized by a ramp-flat thrust fault. As the subduction continued, a layered deformation pattern emerged, with the upper section exhibiting a leading imbricate fan, while the lower section developed four thrust faults.

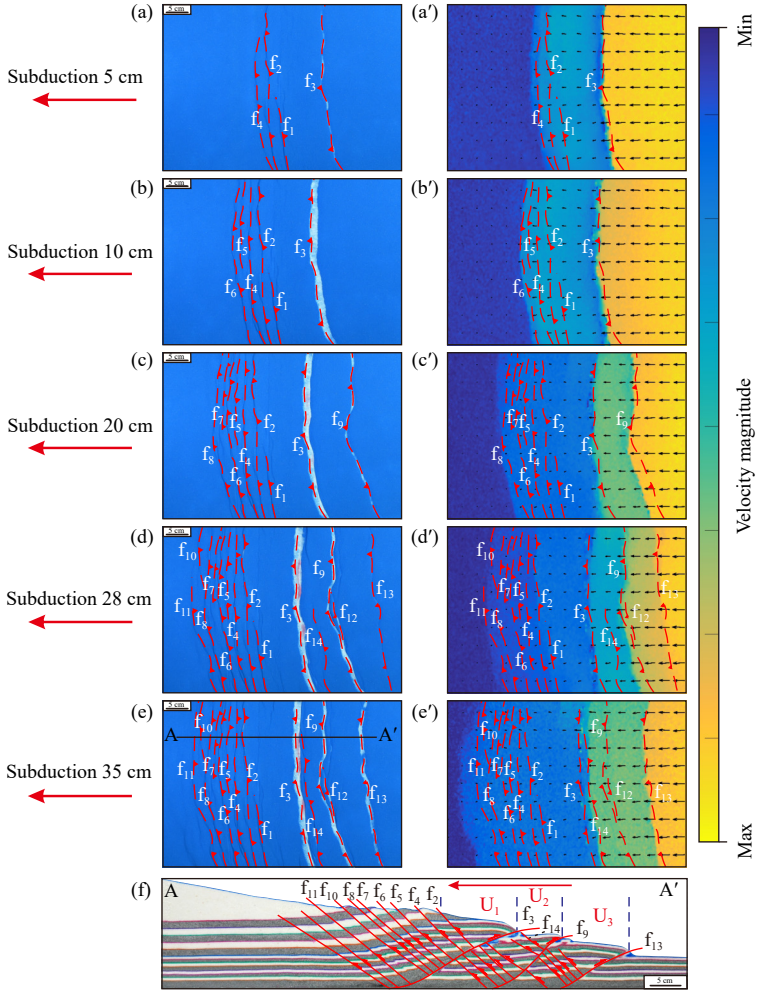

Fig.8 Plan view evolution and section slicing results of Experiment 1. On the left, (a)–(e) show the plan view evolution process during the experiment. On the right, (a′)–(e′) show the plan PIV analysis results of the experiment. At the bottom, (f) shows the section slicing results of the experiment, with the section position indicated in (e). The faults marked in the profile correspond to those visible in the plan view, whereas the unmarked faults in the profile either did not form fully or were not distinctly visible in the plan view.

4.2.1 Experiment 1

The plan view evolution of Experiment 1 is shown in Fig.8, with faults f_1 to f_{14} developing sequentially. During the subduction of 0–5 cm, back thrust faults f_1 and f_2 first developed on the surface of the sand layer at the wedge's front, followed by the sequential formation of forward thrust f_3 and back thrust f_4 (Fig.8a). During the subduction from 5 to 10 cm, the displacement of f_3 increased, and reverse faults f_5 and f_6 formed sequentially (Fig.8b). During the subduction of 10–20 cm, the displacement of f_3 continued to increase, and reverse faults f_7 and f_8 formed in succession. Additionally, a new forward thrust fault f_9 developed at the wedge front (Fig.8c). During the subduction of 20–28 cm, back thrust faults f_{10} and f_{11} formed, along with forward thrusts f_{12} and f_9. Subsequently, forward thrust f_{13} developed at the wedge front, and reverse fault f_{14} formed between f_3 and f_9 (Fig.8d). During the subduction of 28–35 cm, the displacement of f_{13} increased, and faults f_{11} and f_{14} extended along strike, while f_9 and f_{12} gradually approached f_3 (Fig.8e). The results indicate that the wedge front primarily developed forward thrust faults, while the rear part only developed reverse faults. The span of deformation involving back thrust faults was 18.2 cm, with an average spacing of 1.7 cm between the faults. PIV analysis revealed that the sand layers continuously moved leftward during subduction, with velocity gradually decreasing from the wedge front to the rear. When new faults formed at the front, pre-existing

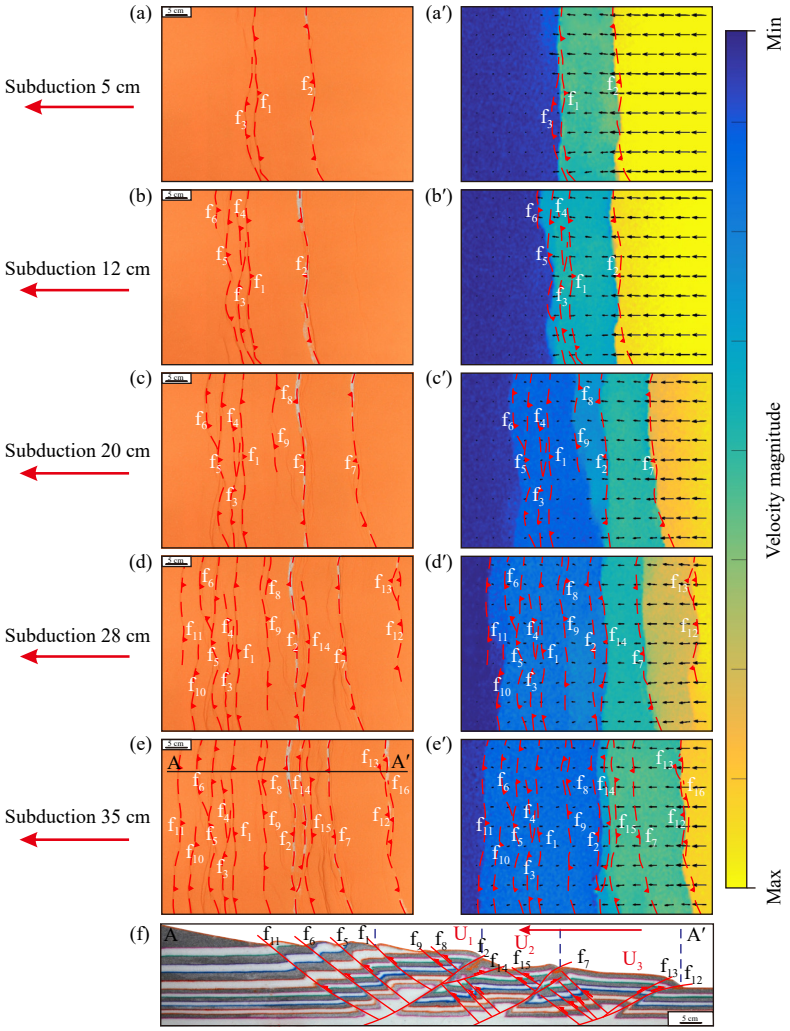

Fig.9 Plan view evolution and section slicing results of Experiment 2. The detailed description is the same as in Fig.8.

faults were reactivated.

The section slicing result of the experiment is shown in Fig.8f, showing that the thrust wedge is composed of three imbricate thrust-fold belts, forming a deformation zone measuring 56.3 cm in length. The widths of structural units U_1, U_2, and U_3 are 12.2 cm, 7.7 cm, and 10.7 cm, respectively, with an average width of 10.2 cm. Combining the plan evolution of the experiment with the section slicing results, it can be concluded that after the experiment began, pop-up structure U_1 formed first. During the following subduction after the formation of fault f_3, the pop-up structure could only absorb a limited amount of strain. Consequently, a portion of the strain was absorbed by fault f_3, leading to an increase in its scale. Some strain was also absorbed by back thrust faults at the rear of the wedge, resulting in the formation of multiple back thrust faults that evolved into imbricate thrust belts and fault-related folds. Structural units U_2 and U_3 generally followed the deformation pattern of U_1. As the forward thrust faults increased, multiple back thrust faults originating from the hanging wall formed imbricate thrust belts. The back thrust fault of structural unit U_1 propagated to the surface of the sand layers, while the back thrust faults of units U_2 and U_3 mainly developed within the wedge and did not propagate to the surface. For structural unit U_3, due to limited subduction, it remained in the pop-up structure stage and had not yet entered the fault-related folding deformation stage. Throughout the subduction process, U_1, U_2, and U_3 remained in an active state.

4.2.2 Experiment 2

The plan view evolution of Experiment 2 is shown in Fig.9, with faults f_1 to f_{16} developing sequentially. The results indicate that some forward thrust faults develop at the wedge front, while back thrust faults develop at the wedge rear. The span of deformation involved in the back thrust faults was 24.5 cm, with an average spacing of 2.3 cm between the faults, which is similar to Experiment 1. However, compared to Experiment 1, the reverse faults at the rear of the wedge in Experiment 2 exhibit larger deformation and wider spacing. PIV analysis revealed that the sand layers continuously moved leftward during subduction, with velocity gradually decreasing from the we dge front to the rear. When new faults form at the front, pre-existing faults are reactivated, similar to the observations in Experiment 1.

The section slicing results of the experiment are shown in Fig.9f, where the thrust wedge is composed of three imbricate thrust-fold belts, forming a deformation zone

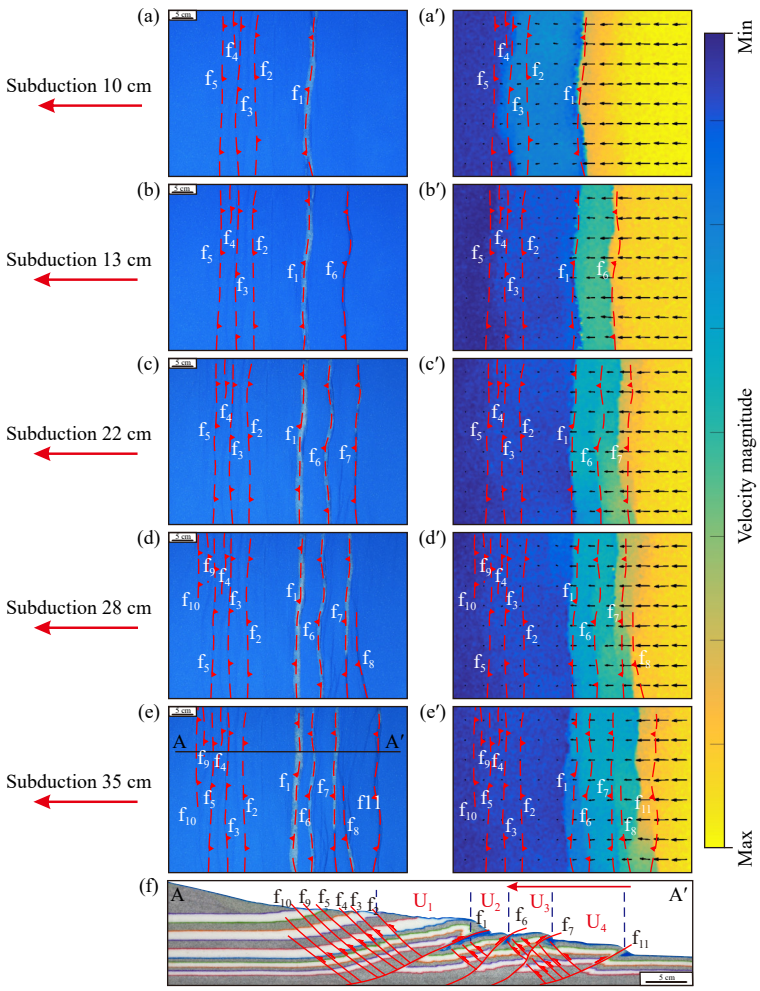

Fig.10 Plan view evolution and section slicing results of Experiment 3. The detailed description is the same as in Fig.8.

measuring 62.2 cm in length. The width of structural units U_1, U_2, and U_3 are 15.9 cm, 14.7 cm, and 14.8 cm, respectively, with an average width of 15.1 cm. The deformation pattern in Experiment 2 is consistent with that of Experiment 1, exhibiting similar deformation styles. The wedge is composed of imbricate thrust belts, sequentially forming U_1, U_2, and U_3. The main difference is that the triangular structural zone in Experiment 2 is wider than that in Experiment 1.

4.2.3 Experiment 3

The plan view evolution of Experiment 3 is shown in Fig.10, with faults f_1 to f_{11} developing sequentially. The results indicate that some forward thrust faults develop at the wedge front, while back thrust faults develop at the wedge rear. The span of deformation involved in the back thrust faults is 10.3 cm, with an average spacing of 1.2 cm between the faults, which is similar to Experiment 1. However, in Experiment 3, four through-going forward thrust faults developed at the wedge front, whereas only three developed in Experiment 1. In Experiment 3, the reverse faults at the rear exhibited a smaller span of deformation, tighter spacing, and straighter patterns compared to those interconnecting overall arc-like faults with larger deformation span and wider spacing in Experiment 1. PIV analysis revealed that the sand layers continuously moved leftward during subduction, with velocity gradually decreasing from the wedge front to the rear. When new faults form at the front, pre-existing faults are reactivated, similar to the observations in Experiment 1.

The section slicing results of the experiment are shown in Fig.10f, where the thrust wedge is composed of four imbricate thrust-fold belts, forming a deformation zone with a length of 43.2 cm. The width of structural units U_1, U_2, U_3, and U_4 are 13.4 cm, 4.6 cm, 5.2 cm, and 9.4 cm, respectively, with an average width of 8.2 cm. The deformation pattern in Experiment 3 is consistent with that of Experiment 1, exhibiting similar deformation styles. The wedge is composed of imbricate thrust-fold belts, sequentially forming U_1, U_2, U_3, and U_4. The main difference is that the wedge in Experiment 3 is composed of four imbricate thrust-fold belts with a smaller triangular structural zone, in contrast to Experiment 1, which is composed of three imbricate thrust-fold belts with a larger triangular structural zone.

4.2.4 Experiment 4

The plan view evolution of Experiment 4 is shown in Fig.11, with faults f_1 to f_{11} developing sequentially. During the subduction of 0–10 cm, the wedge front sequen-

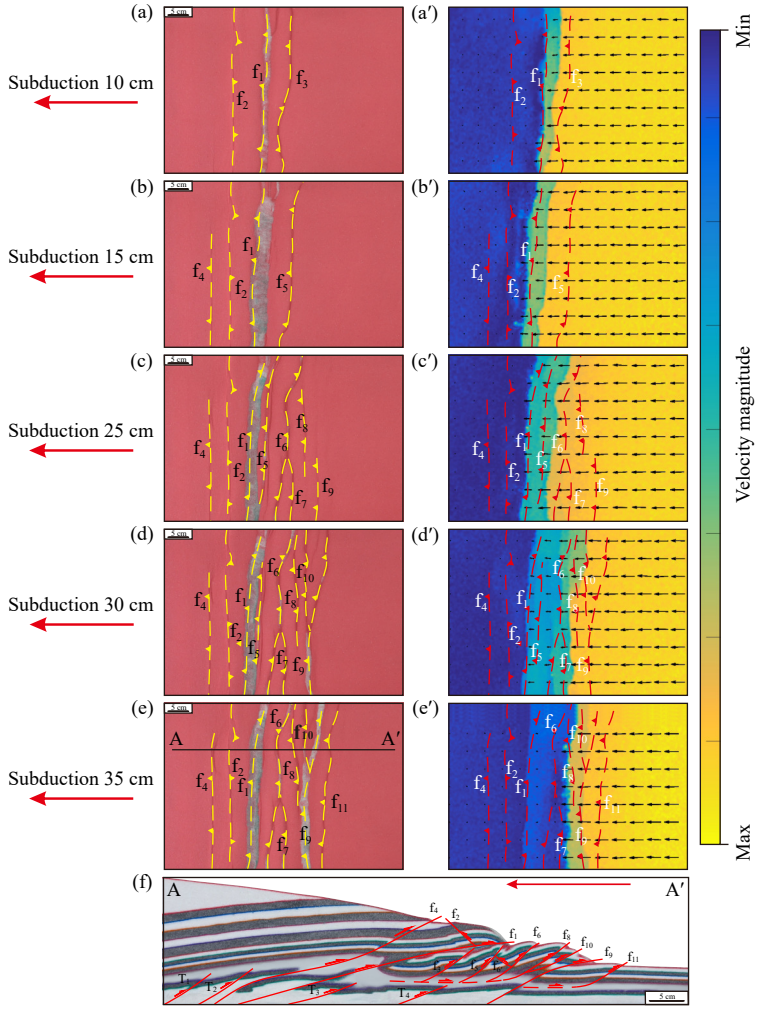

Fig.11 Plan view evolution and section slicing results of Experiment 4. The detailed description is the same as in Fig.8.

tially developed faults f_1, f_2, and f_3 (Fig.11a). During the subduction of 10–15 cm, the displacement of faults f_1 continued to increase, and f_3 gradually approached f_1, eventually merging into a single fault. Then, forward thrust faults f_4 and f_5 were formed sequentially (Fig.11b). During the subduction of 15–25 cm, f_5 moved closer to f_1, and forward thrust faults f_6, f_7, f_8, and f_9 developed sequentially, with f_7 intersecting f_6 (Fig.11c). During the subduction of 25–30 cm, f_5 moved further towards f_1, and f_8 and f_9 extended along strike, with the formation of f_{10} intersecting f_9 (Fig.11d). During the subduction of 30–35 cm, f_5 eventually merged with f_1 into a single fault, followed by the formation of forward thrust fault f_{11} (Fig.11e). The results indicate that deformation in Experiment 4 was mainly concentrated at the wedge front, primarily characterized by forward thrust faults with occasional back thrust faults. In contrast, in Experiment 1, deformation was distributed across both the front and rear of the wedge, with highly developed forward thrust faults at the front and back thrust faults at the rear. PIV analysis revealed that the sand layers continuously moved leftward during subduction, with velocity gradually decreasing from the wedge front to the rear. When new faults form at the front, pre-existing faults are reactivated, similar to the observations in Experiment 1.

The section slicing results of the experiment shown in Fig.11f reveal a thrust wedge with a deformation zone measuring 62.7 cm in length, exhibiting a layered deformation pattern. In the upper section above the decollement layer, forward thrust imbricate faults (f_3, f_5, f_6, f_8) and fault propagation folds developed, with the bases of the imbricate thrust faults converging toward the decollement layer. In the lower section below the decollement layer, four small-displacement thrust faults (T_1, T_2, T_3, T_4) developed. At the wedge front, large ramp-flat thrust fault f_4, large thrust nappe fault f_1, and reverse fault f_9 were observed.

5 Discussion

5.1 Structural Styles of Thrust Wedge

The results of Experiments 1, 2, 3, and 4 reveal that the deformation patterns observed in Experiments 2 and 3 are similar to those in Experiment 1, whereas Experiment 4 exhibits significant differences. In all experiments, the sand layers consistently moved leftward during the subduction process, with velocity decreasing gradually from the frontal edge to the rear of the wedge. As new faults formed at the wedge's front, previously developed faults remained active, reflecting a distributed deformation pat-

tern that collectively accommodated the subduction displacement (Figs.8–11). In Experiments 1, 2, and 3, forward-propagating faults developed at the wedge front, while back thrust faults formed at the rear. Cross-sectional slices revealed that the structural styles were characterized by imbricate thrust-fold belts and fault propagation folds. Initial deformation was activated at the wedge front and evolved into imbricate thrusts and related folds. The frontal thrust faults were most active during their early stages, but their activity gradually diminished as subduction progressed and new thrust faults developed at the wedge front (Fig.12).

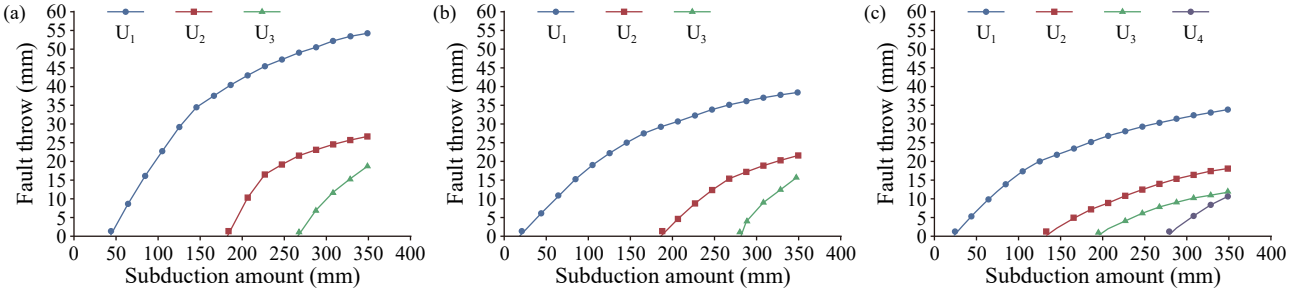

Fig.12 Relationship between the amount of subduction and the uplift height of the pop-up structure. (a), Experiment 1; (b), Experiment 2; (c), Experiment 3.

In comparison to Experiment 1, the initial angle of the wedge was decreased in Experiment 2. Table 3 shows that in Experiment 2, the width of each pop-up structure (U_1, U_2, U_3) significantly increased, with an average width rising from 10.2 cm to 15.1 cm, while the uplift height decreased, with an average height falling from 3.3 cm to 2.6 cm. The deformation range and spacing of the reverse faults at the rear of the wedge increased, with the deformation range expanding from 18.2 cm to 24.5 cm and the spacing widening from 1.7 cm to 2.3 cm. Additionally, both the deformation zone and the overall length of the wedge increased, with the former extending from 56.3 cm to 62.2 cm and the latter from 76.5 cm to 86.4 cm. In summary, the reduction in the initial angle of the wedge led to an increase in the width of the pop-up structures and a decrease in their uplift height, while the deformation range of the reverse faults at the rear expanded and their spacing increased. This facilitated lateral growth of the thrust wedge while restricting vertical growth.

Compared to Experiment 1, the thickness of the horizontal sand layer was reduced in Experiment 3. Table 3 shows that the number of pop-up structures increased in Experiment 3, but their sizes decreased, with the average width reducing from 10.7 cm to 8.2 cm and the average height decreasing from 3.3 cm to 1.8 cm. The deformation range and spacing of the reverse faults at the wedge rear decreased, with the deformation range shrinking from 18.2 cm to 10.3 cm and the spacing narrowing from 1.7 cm to 1.2 cm. At the same time, the overall size of the thrust wedge decreased, with the deformation zone and overall length of the wedge reducing from 56.3 cm to 43.2 cm and from 76.5 cm to 68.7 cm, respectively. In summary, the reduction in the thickness of the horizontal sand layer reduced the size of the pop-up structures but increased their number, while the deformation range of the reverse faults at the rear diminished and their spacing tightened, thus restricting both the lateral and vertical growth of the thrust wedge. These experimental results are consistent with the findings of Mandal *et al*. (1997), which indicate that a reduction in layer thickness decreases the spacing of thrust faults.

In Experiment 4, a 1 cm-thick micro glass bead layer was added within the horizontal sand layer, maintaining the same total sand thickness as in Experiment 1. The results show that the structural style of the wedge in Experiment 4 exhibits a layered deformation pattern. The upper section above the decollement layer develops a forward-propagating imbricate thrust system, with the faults converging at the decollement layer, while the lower part develops small-displacement thrust faults. Table 3 shows that, compared to Experiment 1, the deformation zone length of the wedge in Experiment 4 increased from 56.3 cm to 62.7 cm, but the overall length shortened from 76.5 cm to 72.1 cm. In summary, the decollement layer inhibited the development of reverse faults, enhanced the localized formation of forward thrust faults, limited the lateral

Table 3 Parameter values from the experimental results

Experimental group	Width of the pop-up structure (cm)					Elevation height of the pop-up structure (cm)					Back thrust at the rear edge of the wedge		Deformation zone length (cm)	Total length of the wedge (cm)
	U_1	U_2	U_3	U_4	Average	U_1	U_2	U_3	U_4	Average	Deformation range (cm)	Average spacing (cm)		
Experiment 1	12.2	7.7	10.7	–	10.2	5.4	2.7	1.9	–	3.3	18.2	1.7	56.3	76.5
Experiment 2	15.9	14.7	14.8	–	15.1	3.9	2.1	1.7	–	2.6	24.5	2.3	62.2	86.4
Experiment 3	13.4	4.6	5.2	9.4	8.2	3.4	1.8	1.2	1.1	1.8	10.3	1.2	43.2	68.7
Experiment 4	–	–	–	–	–	–	–	–	–	–	–	–	62.7	72.1

accretion of the wedge, and increased the length of the deformation zone.

Overall, the results of Experiment 4 closely resemble the interpretation of the actual seismic profile (Fig.13) in several aspects:

1) The actual north-south seismic profile reveals multiple parallel or sub-parallel forward thrust faults in the imbricate fan region of the Makran accretionary wedge with occasional back thrust faults. The section slicing results of Experiment 4 shows that the imbricate thrust faults (f_3, f_5, f_6, f_8) include only one back thrust fault ($f_{6'}$).

2) In the actual north-south seismic profile, the spacing between adjacent thrust faults in the imbricate fan region typically ranges from 5 to 8 km, with individual thrust faults exhibiting a listric shape. The section slicing results of Experiment 4 similarly show typical imbricate thrust faults (f_3, f_5, f_6, f_8) with spacings of 6.7 cm, 5.1 cm, and 5.8 cm, corresponding to actual distances of 6.7 km, 5.1 km, and 5.8 km, respectively. The average spacing of 5.9 km is closest to the real situation, and the individual faults also exhibit a listric shape.

3) In the actual north-south seismic profile, layered deformation characteristics are observed, with thrust faults converging downward into the decollement layer. Moreover, a few small-scale thrust faults are developed beneath the detachment layer. Similarly, in Experiment 4, the thrust faults (f_3, f_5, f_6, f_8) also converge into the decollement layer, beneath which four small-scale thrust faults (T_1, T_2, T_3, T_4) are developed.

4) The accretion at the front of the Makran accretionary wedge causes previous developed faults to rotate backward and become reactivated, showing stronger activity in the south and weaker activity in the north. The PIV analysis of Experiment 4 shows that the wedge front moves fastest, with velocity gradually decreasing from the front to the rear of the wedge. When new faults form at the front, pre-existing faults are reactivated; however, their activity diminishes over time.

5.2 Comparison of Experimental Models

The results of Experiment 4 indicate that the forward-propagating imbricate thrust structure of the Makran accretionary wedge develops during oceanic plate subduction, with a decollement layer present at the base. The spacing and arcuate shapes of the thrust faults may be influenced by this decollement layer. The mud diapir structure in the middle slope area may be caused by the load of the rear wedge exerting significant pressure on the lower decollement layer. This pressure, combined with the subduction process, promotes the upward migration of plastic material into low-pressure areas, with the deep thrust faults providing pathways for this movement.

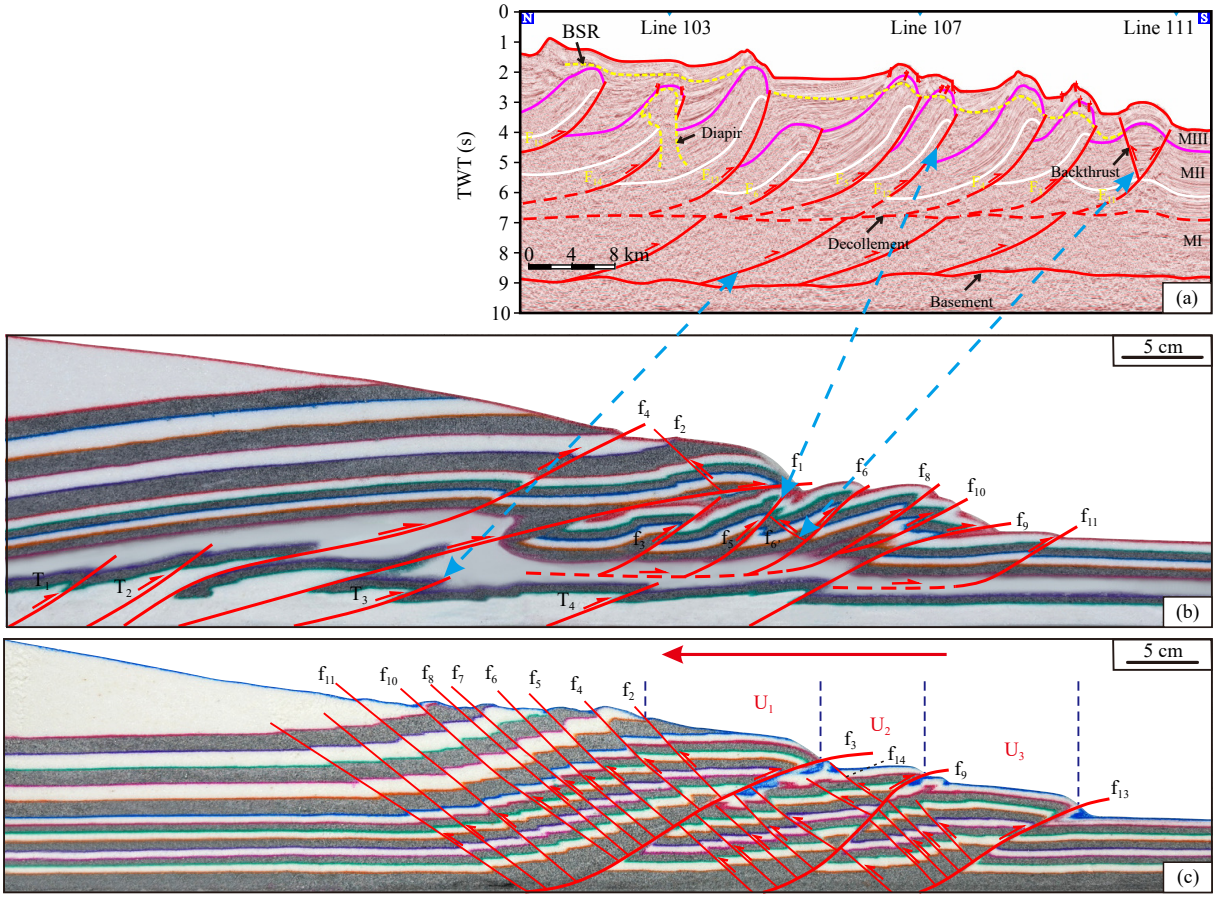

Fig.13 Comparison between actual seismic section interpretation and experimental section interpretation. (a), interpretation of the S-N line 120 seismic section from the Makran accretionary wedge (modified from Shao *et al.*, 2024). The section location is shown in Fig.1. (b), interpretation of the section from Experiment 4. (c), interpretation of the section from Experiment 1.

Previous studies have investigated the structural style of the Makran accretionary wedge through a 'subduction slot' style sandbox experiment (Fig.14a), pointing out that its thrust faults are controlled by a decollement layer (Shao *et al.*, 2024). When comparing the results of the 'subduction slot' style model with those of Experiment 1 in this paper (Figs.14d and 8f), it is important to note that both experiments used the same dry quartz sand without a decollement layer. In the 'subduction slot' model, faults f_1 to f_{13} form sequentially, creating a 'double wedge' structure. Within this structure, the sand bodies thin out and are eliminated in two opposite directions, forming a forward wedge and a reverse wedge. The forward wedge refers to the wedge-shaped body whose direction of elimination is opposite to the subduction direction, characterized by more obvious lateral growth. Conversely, the reverse wedge is the wedge-shaped body whose direction of elimination is the same as the subduction direction. At a subduction amount of 30 cm, the forward-propagating imbricate thrust belt (U_1) is controlled by fault f_2, while the triangular structural zone (U_2), controlled by fault f_{10}, begins to form at 26.5 cm. The uplift heights of U_1 and U_2 are 4.5 cm and 0.75 cm, respectively. In comparison, Experiment 1 in this paper formed three imbricate thrust belts (U_1, U_2, U_3) at a subduction amount of 35 cm, with uplift heights of 5.4 cm, 2.7 cm, and 1.9 cm, respectively. From this point, it can be concluded that the 'wedge' style model exhibits a more similar deformation pattern to that observed in the actual seismic interpretation (Fig.13).

In the 'subduction slot' style model, deformation is concentrated around the subduction slot, and a few of the back thrusts develop to form retro-wedge structure (McClay *et al.*, 2004). In contrast, in the 'wedge' style model, deformation propagates forward from the wedge front, and the back thrusts within the imbricate thrust-fold belt are inclined opposite to the subduction direction. A comprehensive comparison reveals that the thrust faults (f_3, f_9, f_{13}) in the 'wedge' style model are more similar to the thrust faults observed in the downslope region of the actual seismic profile (Figs.13 and 14). It can be inferred that the formation of thrust faults at the front of the Makran accretionary wedge is controlled by a bounding wedge. The triangular structural zone that forms later in the 'subduction slot' style model is similar to the early structural

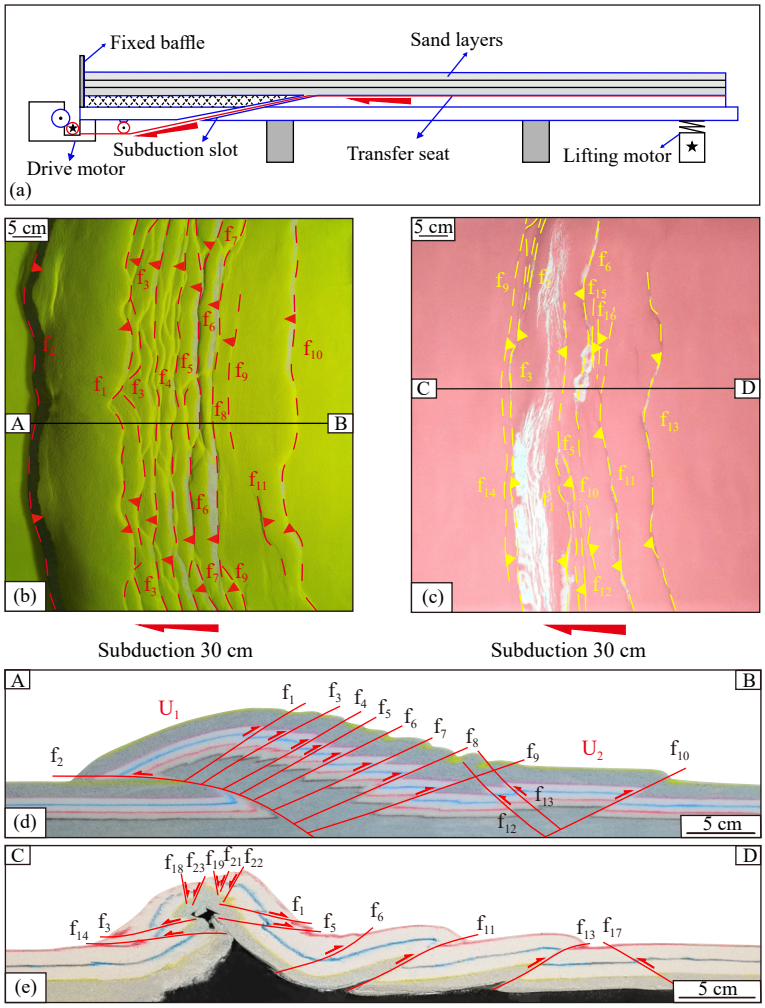

Fig.14 Experimental device and experimental result interpretation in a 'subduction slot' model (Shao *et al.*, 2024). (a), experimental device; (b) and (c), experimental interpretation in plan view, with black horizontal lines indicating the section locations and red arrows indicating the subduction direction; (d), interpretation of the section from the 'subduction slot' model experiment without a detachment layer at the base; (e), interpretation of the section from the 'subduction slot' model experiment with a detachment layer at the base.

style observed in Experiment 1 of this paper. This suggests that, in the absence of a decollement layer, the 'subduction slot' style model first forms a large-scale imbricate thrust-fold belt as a bounding wedge, and subsequently, the structural style at the front of the forward wedge gradually becomes consistent with that observed in Experiment 1 of this paper.

5.3 Significance of Thrust Imbricate Faults in the Makran Accretionary Wedge for Gas Hydrates

The imbricate thrust faults within the Makran accretionary wedge play a crucial role in the structural control of gas hydrate reservoirs. Firstly, these thrust faults provide vertical migration pathways for deep-seated fluids, allowing gas to ascend through the thrust faults and accumulate at structural highs. The effectiveness of these fluid migration pathways determines the degree of gas hydrate enrichment within specific structural units (Gong *et al*., 2018b; Liao *et al*., 2022). Secondly, the thrust faults create compressive anticlines and associated structural traps in the hanging wall, offering favorable conditions for the stable presence of gas hydrates. In the context of low-angle subduction, the thrust faults, together with shallow normal faults, form a multi-tiered fluid migration system, which controls the distribution and accumulation of gas within the sedimentary layers (Smith, 2012; Gong *et al*., 2018a; Meng *et al*., 2019), giving rise to a predictable hydrate reservoir pattern.

In summary, the thrust imbricate structures in the Makran accretionary wedge are not only key components of tectonic deformation in subduction zones but also play a significant role in the formation and accumulation of gas hydrates. A deeper understanding of these thrust imbricate faults can help to improve reservoir prediction accuracy and, thereby, enhance economic benefits.

6 Conclusions

1) In the absence of a decollement layer, decreasing the initial wedge angle and thinning the horizontal sand layer has little impact on the wedge's structural style. However, when a decollement layer is present within the horizontal sand layer, the wedge's structural style exhibits layered deformation. The upper section develops a forward-propagating imbricate thrust structure, with thrust faults converging at the decollement layer, while the lower part develops smaller thrust faults.

2) When the initial wedge angle is reduced from 11° to 8°, the width of the pop-up structures increases, while their uplift height decreases, leading to greater lateral growth of the thrust wedge and less vertical growth. Additionally, the reduction in the initial wedge angle results in larger deformation scales and wider spacing of the back thrust faults at the wedge rear.

3) When the thickness of the horizontal sand layer is reduced from 4.5 cm to 3 cm, both the width and uplift height of the pop-up structures decrease. The spacing of the forward thrust faults decreases, while their number increases. Both lateral and vertical growth relatively decrease, resulting in a smaller thrust wedge. Simultaneously, the reduction in horizontal sand layer thickness decreases the deformation scale of the back thrust faults at the wedge rear, with the fault spacing becoming closer.

4) The decollement layer suppresses the development of back thrust faults and enhances the localized formation of forward thrust faults at the wedge front. It also limits the lateral accretion of the overall wedge length while increasing the length of the wedge deformation zone.

5) Comprehensive comparisons show that the thrust imbricate faults at the front of the Makran accretionary wedge are primarily controlled by the occurrence of the wedge and the decollement layer within the sediments of the oceanic crust.

Acknowledgement

This study was funded by the National Natural Science Foundation of China (No. 42076069).

Author Contributions

Bo Sun: conducted the literature review, contributed to the experimental design, and drafted the initial version of the manuscript. Fusheng Yu: submitted the manuscript to the journal and handled all communication with the editorial office, including responding to reviewers' comments and overseeing manuscript revisions; ensured the accuracy and integrity of the content, verified all co-authors' information, contributions, and authorship order; coordinated communication among the authors and ensured that all co-authors reviewed and approved the final version of the manuscript prior to submission and publication. After publication, the corresponding author is also responsible for responding to any inquiries regarding the data, methodology, or findings, and for providing data upon reasonable request. Jing Liao and Jianming Gong: processed and interpreted the seismic data. Jiajie Yan, Wenhao Lei, Jiajun Qu, Haoyue Sun and Jia Ren: participated in the execution of the physical simulation experiments. Zixuan Cui: revised and polished the manuscript language.

Data Availability

The data and references presented in this study are available from the corresponding author upon reasonable request.

Declarations

Ethics Approval and Consent to Participate

This article does not contain any studies with human participants or animals performed by any of the authors.

Consent for Publication

Informed consent for publication was obtained from all

participants.

Conflict of Interests

The authors declare that they have no conflict of interests.

Open Access

References

Arthurton, R. S., Farah, A., and Ahmed, W., 1982. The late Cretaceous-Cenozoic history of western Baluchistan Pakistan–The northern margin of the Makran subduction complex. *Geological Society, London, Special Publications*, **10** (1): 373–385.

Avouac, J. P., and Burov, E., 1996. Erosion as a driving mechanism of intracontinental mountain growth. *Journal of Geophysical Research: Solid Earth*, **101** (B8): 17747–17769.

Barbero, E., Pandolfi, L., Delavari, M., Dolati, A., Saccani, E., Rosa, M. D., *et al*., 2025. A review of Mesozoic geodynamic evolution of the North Makran (SE Iran): A tale of a Neo-Tethyan Ocean vanished due to two coexisting subduction zones. *Gondwana Research*, **141**: 74–101.

Burg, J. P., 2018. Geology of the onshore Makran accretionary wedge: Synthesis and tectonic interpretation. *Earth-Science Reviews*, **185**: 1210–1231.

Cotton, J. T., and Koyi, H. A., 2000. Modeling of thrust fronts above ductile and frictional detachments: Application to structures in the Salt Range and Potwar Plateau, Pakistan. *Geological Society of America Bulletin*, **112** (3): 351–363.

Cromie, C., Scarselli, N., Craig, J., Khan, M. R., and Hussain, A., 2022. Tectonostratigraphic evolution and hydrocarbon prospectivity south of Gwadar Bay, Makran accretionary wedge, offshore SW Pakistan. *Journal of Petroleum Geology*, **45** (2): 179–199.

Davis, D., Suppe, J., and Dahlen, F. A., 1983. Mechanics of fold-and-thrust belts and accretionary wedges. *Journal of Geophysical Research: Solid Earth*, **88** (B2): 1153–1172.

Demets, C., Gordon, R. G., Argus, D., and Stein, S., 1990. Current plate motions. *Geophysical Journal International*, **101** (2): 425–478.

Ding, F., Spiess, V., Fekete, N., Murton, B., Brüning, M., and Bohrmann, G., 2010. Interaction between accretionary thrust faulting and slope sedimentation at the frontal Makran accretionary prism and its implications for hydrocarbon fluid seepage. *Journal of Geophysical Research: Solid Earth*, **115** (B8): 1–16.

Dominguez, S., Lallemand, S., Malavieille, J., and Von Huene, R., 1998. Upper plate deformation associated with seamount subduction. *Tectonophysics*, **293** (3–4): 207–224.

Ellouz-Zimmermann, N., Deville, E., Müller, C., Lallemant, S., Subhani, A. B., and Tabreez, A. R., 2007. Impact of sedimentation on convergent margin tectonics: Example of the Makran accretionary prism (Pakistan). In: *Thrust Belts and Foreland Basins: From Fold Kinematics to Hydrocarbon Systems*. Lacombe, O., *et al*., eds., Springer, Berlin Heidelberg, 327–350.

Fruehn, J., White, R., and Minshull, T., 1997. Internal deformation and compaction of the Makran accretionary wedge. *Terra Nova*, **9** (3): 101–104.

Gaedicke, C., Prexl, A., Schlüter, H. U., Meyer, H., Roeser, H., and Clift, P., 2002. Seismic stratigraphy and correlation of major regional unconformities in the northern Arabian Sea. *Geological Society, London, Special Publications*, **195** (1): 25–36.

Gong, J. M., Liao, J., Sun, J., Yang, C. S., Wang, J. Q., He, Y. J., *et al*., 2016. Factors controlling gas hydrate accumulation in Makran accretionary wedge of Pakistan. *Marine Geology Frontiers*, **32** (12): 10–15.

Gong, J. M., Liao, J., Yin, W. H., Zhang, L., He, Y. J., Sun, Z. L., *et al*., 2018a. Gas hydrate accumulation models of Makran accretionary wedge, northern Indian Ocean. *Marine Geology and Quaternary Geology*, **38** (2): 148–155.

Gong, J. M., Liao, J., Zhang, L., He, Y. J., Zhai, B., Meng, M., *et al*., 2018b. Discussion on the distribution and main controlling factors of mud volcanoes in Makran accretionary wedge. *Geoscience*, **32** (5): 1025–1030.

Grando, G., and McClay, K., 2007. Morphotectonics domains and structural styles in the Makran accretionary prism, offshore Iran. *Sedimentary Geology*, **196** (1–4): 157–179.

Hampel, A., Adam, J., and Kukowski, N., 2004. Response of the tectonically erosive south Peruvian forearc to subduction of the Nazca Ridge: Analysis of three-dimensional analogue experiments. *Tectonics*, **23** (5): TC5003.

Harms, J. C., Cappel, H. N., and Francis, D. C., 1984. The Makran coast of Pakistan: Its stratigraphy and hydrocarbon potential. In: *Marine Geology and Oceanography of Arabian Sea and Coastal Pakistan*. Haq, B. U., and Milliman, J. D., eds., U.S. Department of Energy Office of Scientific and Technical Information, Washington, D. C., 3–27.

Hoth, S., 2005. Deformation, erosion and natural resources in continental collision zones: Insight from scaled sandbox simulations. PhD thesis. Freien Universität Berlin, Potsdam.

Hoth, S., Adam, J., Kukowski, N., and Oncken, O., 2006. Influence of erosion on the kinematics of bivergent orogens. Results from scaled sandbox simulations. In: *Tectonics, Climate and Landscape Evolution*. Willett, S., *et al*., eds., Geological Society of America, Boulder, 201–225.

Khan, M. R., Hussain, A., Sajid, M., and Javed, T., 2015. Mud diapirism induced structuration and implications for the definition and mapping of hydrocarbon traps in Makran accretionary prism. AAPG/SEG International Conference & Exhibition, Washington, D. C., 13–16.

Konstantinovskaia, E., and Malavieille, J., 2005. Erosion and exhumation in accretionary orogens: Experimental and geological approaches. *Geochemistry, Geophysics, Geosystems*, **6** (2): 1–25.

Kopp, C., Fruehn, J., Flueh, E., Reichert, C., Kukowski, N., Bialas, J., *et al*., 2000. Structure of the Makran subduction

zone from wide-angle and reflection seismic data. *Tectonophysics*, **329** (1–4): 171–191.

Koyi, H., Jenyon, M., and Petersen, K., 1993. The effect of basement faulting on diapirism. *Journal of Petroleum Geology*, **16** (3): 285–312.

Kukowski, N., Schillhorn, T., Huhn, K., Von Rad, U., Husen, S., and Flueh, E. R., 2001. Morphotectonics and mechanics of the central Makran accretionary wedge off Pakistan. *Marine Geology*, **173** (1–4): 1–19.

Lallemand, S. E., Malavieille, J., and Calassou, S., 1992. Effects of oceanic ridge subduction on accretionary wedges: Experimental modeling and marine observations. *Tectonics*, **11** (6): 1301–1313.

Liao, J., Gong, J. M., He, Y. J., Yue, B. J., and Meng, M., 2019. Markland accretionary wedge sequence and development process. *Marine Geology Frontiers*, **35** (4): 69–72.

Liao, J., Liu, X., Zhao, Q., Gong, J., Yin, W., Li, S., *et al*., 2022. Characteristics of high saturation hydrate reservoirs in the low-angle subduction area of the Makran accretionary prism. *Frontiers in Earth Science*, **10**: 861162.

Mandal, N., Chattopadhyay, A., and Bose, S., 1997. Imbricate thrust spacing: Experimental and theoretical analyses. In: *Evolution of Geological Structures in Micro- to Macro-Scales*. Sengupta, S., ed., Chapman and Hall, London, 143–165.

McClay, K. R., and Whitehouse, P. S., 2004. Analog modeling of doubly vergent thrust wedges. In: *Thrust Tectonics and Hydrocarbon Systems*. McClay, K. R., ed., AAPG, New York, 184–206.

Meng, M., Gong, J. M., Liao, J., Pan, J., and He, Y. J., 2019. The study of reservoir formation model promotes the new discovery of gas hydrate investigation. *Marine Geology Frontiers*, **35** (11): 74–76.

Monsef, I., Rahgoshay, M., Pirouz, M., Chiaradia, M., Grégoire, M., and Ceuleneer, G., 2018. The eastern Makran ophiolite (SE Iran): Evidence for a late Cretaceous fore-arc oceanic crust. *International Geology Review*, **61** (11): 1313–1339.

Platt, J., 1986. Dynamics of orogenic wedges and the uplift of high-pressure metamorphic rocks. *Geological Society of America Bulletin*, **97** (9): 1037–1053.

Platt, J., Leggett, J., Young, J., Raza, H., and Alam, S., 1985. Large-scale sediment underplating in the Makran accretionary prism, Southwest Pakistan. *Geology*, **13** (7): 507–511.

Qian, X., Zhang, L., Wu, S., Sun, Z., Lei, Z., and Luo, S., 2022. Seismic characteristics and hydrocarbon accumulation associated with mud diapir structures in a superimposed basin in the southern South China Sea margin. *Journal of Ocean University of China*, **21** (4): 861–875.

Saccani, E., Delavari, M., Dolati, A., Marroni, M., Pandolfi, L., Chiari, M., *et al*., 2018. New insights into the geodynamics of Neo-Tethys in the Makran area: Evidence from age and petrology of ophiolites from the Coloured Mélange Complex (SE Iran). *Gondwana Research*, **62**: 306–327.

Shao, L., Yu, F., Gong, J., Liao, J., Yu, Z., Tang, L., *et al*., 2024. Genetic analysis of structural styles in the Makran accretionary wedge–Insight from physical simulations. *Journal of Ocean University of China*, **23** (1): 157–172.

Smith, G., McNeill, L., Henstock, T. J., and Bull, J., 2012. The structure and fault activity of the Makran accretionary prism. *Journal of Geophysical Research: Solid Earth*, **117** (B7): B07407.

Smith, G. L., McNeill, L. C., Henstock, T. J., Arraiz, D., and Spiess, V., 2014. Fluid generation and distribution in the highest sediment input accretionary margin, the Makran. *Earth and Planetary Science Letters*, **403**: 131–143.

Von Rad, U., Berner, U., Delisle, G., Doose-Rolinski, H., Fechner, N., Linke, P., *et al*., 2000. Gas and fluid venting at the Makran accretionary wedge off Pakistan. *Geo-Marine Letters*, **20** (1): 10–19.

Wang, Z. X., 1995. Formation and evolution of thrust in the wedge of subduction zone: Experiment research on tectonophysics modeling. *Acta Geoscientia Sinica*, **2**: 165–176 (in Chinese with English abstract).

White, R., and Klitgord, K., 1976. Sediment deformation and plate tectonics in the Gulf of Oman. *Earth and Planetary Science Letters*, **32** (2): 199–209.

Willett, S. D., 1992. Dynamic and kinematic growth and change of a Coulomb wedge. In: *Thrust Tectonics*. McClay, K. R., ed., Chapman & Hall, London, 19–31.

Yu, F., Li, D., Zhao, J., and Dong, C., 2012. Physical simulation of double decollements: Insights into the fold-and-thrust belt in the southern front of Junggar Basin. *Journal of Earch Sciences and Environment*, **34** (2): 15–23 (in Chinese with English abstract).

Yu, F., Wang, X., Qiu, X., Wang, D., Li, C., Lv, X., *et al*., 2019. Characteristics of fault structure and the genesis of herringbone structure in Lufeng sag, Pearl River Mouth. *Acta Petrolei Sinica*, **40** (S1): 166–177 (in Chinese with English abstract).

Yu, F., Zhang, R., Yu, J., Wang, Y., Chen, S., Liu, J., *et al*., 2022. Meso-Cenozoic negative inversion model for the Linhe depression of Hetao Basin, China. *Geological Magazine*, **159** (4): 535–560.

(Edited by Chen Wenwen)